Photoemission, resonant photoemission, and x-ray absorption of a Ru(II) complex adsorbed on rutile Ti O 2 (110) prepared by in situ electrospray deposition

Louise C. Mayor, J. Ben Taylor, Graziano Magnano, Anna Rienzo, Christopher J. Satterley, James N. O'Shea, and Joachim Schnadt

Photoemission, resonant photoemission, and x-ray absorption of a Ru(II) complex adsorbed on rutile TiO$_2$(110) prepared by *in situ* electrospray deposition

Louise C. Mayor,[1] J. Ben Taylor,[1] Graziano Magnano,[1] Anna Rienzo,[1] Christopher J. Satterley,[1] James N. O'Shea,[1,a)] and Joachim Schnadt[2]

[1]*School of Physics and Astronomy, University of Nottingham, Nottingham NG7 2RD, United Kingdom*
[2]*Department of Synchrotron Radiation, Lund University, S-221 00 Lund, Sweden*

An experimental study of the bonding geometry and electronic coupling of cis-bis(isothiocyanato)bis(2,2′-bipyridyl-4,4′-dicarboxylato)-ruthenium(II) (N3) adsorbed on rutile TiO$_2$(110) is presented, along with supporting theoretical calculations of the bonding geometry. Samples were prepared *in situ* using ultrahigh vacuum electrospray deposition. Core-level photoemission spectroscopy was used to characterize the system and to deduce the nature of the molecule-surface bonding. Valence band photoemission and N 1s x-ray absorption spectra were aligned in a common binding energy scale to enable a quantitative analysis of the bandgap region. A consideration of the energetics in relation to optical absorption is used to identify the photoexcitation channel between the highest occupied and lowest unoccupied molecular orbitals in this system, and also to quantify the relative binding energies of core and valence excitons. The core-hole clock implementation of resonant photoemission spectroscopy is used to reveal that electron delocalization from N3 occurs within 16 fs. © *2008 American Institute of Physics*.
[DOI: 10.1063/1.2975339]

I. INTRODUCTION

Dye-sensitized solar cells[1] (DSCs) have many practical advantages over traditional inorganic solar cells, and their efficiency is now proving to be competitive when tested with realistic outdoor conditions.[2] In an effort to develop DSCs to their full potential, it is important to understand the subtle electronic properties that enable a high incident-photon-to-current conversion efficiency. The system studied presently is the dye complex (cis-bis(isothiocyanato)bis(2,2′-bipyridyl-4,4′-dicarboxylato)-ruthenium(II) (N3), also referred to as "Ru-535," adsorbed on rutile TiO$_2$(110).[3] This dye, shown in Fig. 1, is of particular importance because it is the most efficient sensitizer for DSCs to date.[4]

N3 has been studied using photoemission of *ex situ* prepared monolayers on TiO$_2$(110) surfaces.[5,6] No *in situ* prepared study of this system has been achieved yet, however, since the dye is too thermally labile to be evaporated in vacuum. Using an ultrahigh vacuum (UHV) electrospray deposition system we can form monolayers and multilayers of the dye on a well-defined TiO$_2$(110) surface. The instrument, developed in-house, allows nonvolatile molecules to be deposited at pressures between 1×10^{-7} and 1×10^{-9} mbar. Thus the surface cleanliness of the TiO$_2$(110) substrate is preserved, with the possible exception of some hydroxylation of the bridging O atoms due to residual water in the UHV chamber,[7] which is not expected to influence the binding of the dye to the Ti atoms. Molecules shown to have been successfully deposited using this technique include

polymers,[8,9] biomolecules,[10] carbon nanotubes,[11] and C$_{60}$,[12,13] and—in the present case—the first *in situ* deposition of N3 on rutile TiO$_2$(110). Real DSC devices are based on the adsorption of the dye to the surface of nanostructured anatase TiO$_2$. However, the adsorption geometry of the primary binding ligand (bi-isonicotinic acid) to the surfaces of both rutile TiO$_2$(110) (Ref. 14) and anatase TiO$_2$(101) (Ref. 15) is of essentially the same character, and the optical band-gaps of the different phases are close at 3.05 (Ref. 16) and 3.20 eV,[17] respectively. The study of N3 adsorbed *in situ* on a rutile TiO$_2$(110) surface under UHV conditions therefore provides a unique opportunity to study the underlying chemical physics of DSCs in detail using photoemission spectros-

FIG. 1. (Color online) (a) N3 molecule adsorbed on TiO$_2$, calculated using CASTEP (Ref. 23) at the DFT-GGA level (see text for details), and (b) chemical structure of the N3 molecule.

Ruthenium · Carbon · Oxygen · Hydrogen · Nitrogen · Sulphur · Titanium
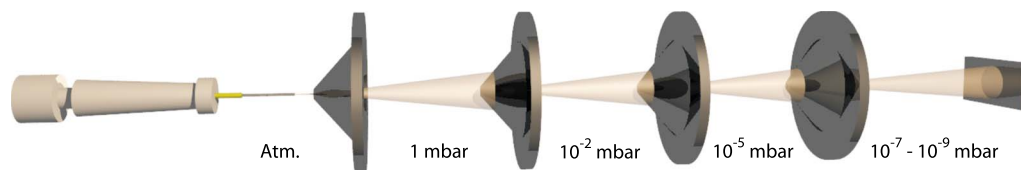
a)Electronic mail: james.oshea@nottingham.ac.uk.

FIG. 2. (Color online) Schematic of the electrospray system showing the molecular beam traveling from left to right as it leaves the high voltage hollow needle, passes via apertures through differentially pumped chambers, and is incident upon the sample.

copy (PES), near-edge x-ray absorption fine structure (NEXAFS) spectroscopy, and resonant PES (RPES). These techniques enable us to probe the occupied and unoccupied states of the system in relation to the substrate conduction band and allow us to gain an insight into the charge-transfer processes that underpin DSCs.

II. EXPERIMENT

Experiments were carried out at the surface science undulator beamline I511-1 (Ref. [18]) at MAX II, MAX-lab in Lund, and at the SRS Daresbury, UK, at beamline MPW6.1. All data presented here is from beamline I511-1, while PES and NEXAFS data were collected at Daresbury for comparison. The I511-1 end station is equipped with a Scienta R4000 electron analyzer that can be rotated orthogonally around the beam axis. A horizontal orientation with the analyzer in-line with the light polarization vector **E** was used for XPS because the maximum flux of direct photoemission electrons ejected from a sample occurs in this direction. For NEXAFS and RPES, however, Auger electrons are collected in preference over direct photoemission electrons, so for these measurements the analyzer was oriented perpendicular to **E**. In both cases, the sample was oriented near to normal emission, which corresponds to 7° off normal due to the grazing incidence geometry of the sample holder.

The rutile $TiO_2(110)$ substrate (Pi-Kem, UK) was clamped to a Ge crystal used for resistive heating of the substrate. Cycles of sputtering and annealing to $\sim 600\,^\circ C$ were used to prepare the surface. As an initial step, repeated cycles were performed in order to change the TiO_2 from an insulator to a n-type semiconductor through the introduction of bulk defects[19] necessary to avoid sample charging. The substrate was deemed clean when it showed a negligible C 1s core-level signal, and the extent of surface defects—which induce states within the bandgap—was kept in check by monitoring the valence band PES.

The N3 molecule (Solaronix SA, Switzerland) was deposited by in situ UHV electrospray deposition. A solution of ~ 5 mg of N3 in 200 ml of a 3(methanol):1(water) mixture was held in a sealed reservoir under an applied pressure of 0.5 bar N_2. This positive pressure pushes the solution from its container through a length of PEEK (polyetheretherketone) tubing with inner diameter (ID) of 860 μm, a stainless steel tube with ID of 250 μm, and finally, a hollow stainless steel needle with ID of 100 μm (New Objective, USA), which was held at a potential of 2.3 kV relative to the ground. Within the needle the solvent becomes ionized, causing the liquid to draw out from the tip to form a Taylor cone.[20] At a threshold voltage, Coulomb repulsion forces

overcome the liquid's surface tension and a jet of droplets is emitted. Solvent molecules then evaporate from these droplets, increasing their charge density and causing them to split repeatedly in a process known as Coulomb explosion.[21] As neutral solvent molecules evaporate from the droplets, the residual charge is imparted (in the complete desolvation limit) to the molecule.

Directly in front of the needle at a distance of ~ 2 mm is a conical entrance aperture with diameter of 0.5 mm, leading to a series of differentially pumped apertures, as shown in Fig. 2. All the apertures are grounded and increase in diameter from 0.5 to 1.0 mm toward the preparation chamber. Between depositions, the electrospray system was sealed off from the preparation chamber using an UHV gate valve. With the valve open but the needle voltage turned off and thus no electrospray process occurring, the pressure in the preparation chamber was 4×10^{-8} mbar. With the needle voltage applied the preparation chamber pressure increased to 2×10^{-7} mbar, the additional pressure being largely due to residual solvent molecules in the molecular beam. The flux of N3 molecules at the sample is approximately 0.1 ML min^{-1}, while the partial pressure of methanol during the deposition is estimated to be in the high 10^{-8} mbar range. The sample was optically aligned with the electrospray system using a laboratory light source.

For the electron spectroscopy data, the total instrument resolution ranges from 40 to 330 meV for PES and from 90 to 170 meV for NEXAFS and RPES. All PES spectra have been calibrated to the substrate O 1s peak at 530.05 eV,[22] and a Shirley background was subtracted before curve fitting using Voigt functions. NEXAFS and RPES spectra were taken over the N 1s absorption edge and were measured using the electron analyzer. For NEXAFS, the surface sensitive nitrogen Auger yield was used for the monolayer, and the deeper-probing secondary electron yield was used for the multilayer. For the RPES data, the photon energy was scanned over the N 1s absorption edge while measuring the valence band photoemission. NEXAFS and RPES spectra were normalized to the photon flux. To avoid beam damage of the molecules under irradiation by soft x rays, the sample was moved continuously to effectively raster the beam across the surface.

Density functional theory (DFT) calculations were carried out as an aid to understanding the experimental data. The $N3/TiO_2(110)$ bonding geometry was optimized using CASTEP (Ref. [23]) at the DFT-generalized gradient approximation (DFT-GGA) level with a plane wave basis set cut off of 300 eV and the Perdew–Burke–Ernzerhof functional. Atoms in the substrate were constrained to their DFT-optimized bulk lattice positions, while atoms in the molecule were un-

TABLE I. BEs (eV) calibrated to the substrate O 1s peak at 530.05 eV (Ref. 22).

		Monolayer	Multilayer
PES			
O 1s	TiO$_2$	530.05	530.05
	C=O and COO$^-$	531.5	531.5
	C—OH	533.1	533.1
S 2p	Bonded	162.4	$\cdots$
	Nonbonded	161.7	161.8
C 1s	Pyridine	285.0	284.8
	Thiocyanate	286.0	285.8
	Carboxyl	288.6	288.6
Ru 3d		280.6	280.4
N 1s	Thiocyanate	397.8	397.6
	Pyridine	399.8	399.7
Valence band	HOMO	1.0	$\cdots$
N 1s NEXAFS			
Unshifted	LUMO	0.3	$\cdots$
Aligned to optical data	LUMO	−1.3	$\cdots$

constrained and optimized using a BFGS algorithm. The same parameters were used to obtain the free molecule geometry, which was then used to calculate the molecular orbitals.

III. RESULTS AND DISCUSSION

The samples used for the following spectra are classed as either *monolayer* or *multilayer*. Here a monolayer is classed as a sample having the vast majority of molecules directly adsorbed to the surface and a multilayer as having a film of molecules thick enough that the majority of photo-electrons in PES come from molecules above the first adsorbed layer. Using the O 1s and S 2p PES spectra, the multilayer is estimated to be between two and three layers thick. Binding energies (BEs) of the peaks discussed are summarized in Table I.

A. Bonding

Figure 3 shows the O 1s photoelectron spectra of the monolayer and multilayer, measured using $h\nu = 600$ eV. For the monolayer, the TiO$_2$ substrate oxygen peak dominates the spectrum. The two smaller peaks are due to the carboxyl O in the bi-isonicotinic acid ($4,4'$-dicarboxy-$2,2'$-bipyridine) ligands of the N3 molecule. For isolated N3, two equally intense O 1s peaks are expected due to the equivalent number of carbonyl (C=O) and hydroxyl (C—OH) oxygen atoms (4:4). In the multilayer, these two molecular O 1s peaks are indeed approximately equal in intensity, implying that the majority of the detected photoelectrons come from N3 molecules with negligible intermolecular and molecule-surface bonding through the bi-isonicotinic acid ligands.

In previous studies, bi-isonicotinic acid has been found to bond to TiO$_2$ through deprotonation of the carboxyl groups, in a 2M-bidentate structure.[14,22,24] This is a common bonding arrangement for pyridine carboxylic acids on the TiO$_2$ surface.[25–27] Once a carboxyl group has deprotonated,
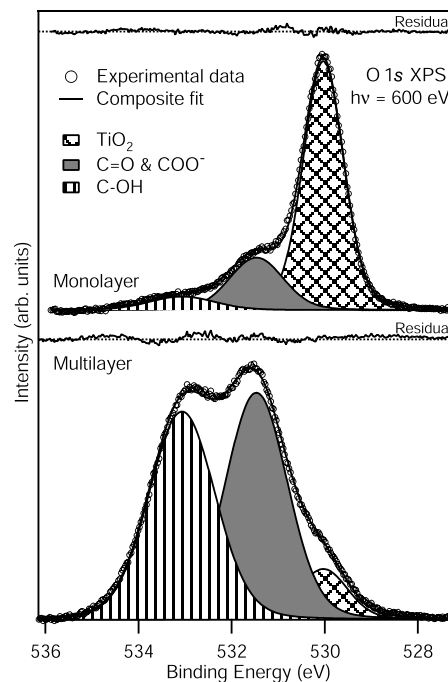
FIG. 3. O 1s core-level spectra measured using $h\nu = 600$ eV. Total instrument resolutions were ~180 and 340 meV for the mono- and multilayers, respectively.

the two O atoms share an electron and are chemically equivalent. The BE of this O species is similar to that of the carbonyl O in the isolated molecule.[14] The COO and COO$^-$ and C=O:C—OH intensity ratio found for the monolayer is 3.2:1. Assuming that all molecules are bonded to the surface in an equivalent way, this is very close to the 3:1 ratio, which would be expected if each molecule has two carboxyl groups bonded to the surface.

Figure 4 shows S 2p photoelectron spectra of the monolayer and multilayer, measured using $h\nu = 225$ eV. Along with the O 1s PES spectra, the S 2p PES spectra are indicative of the bonding of N3 to the TiO$_2$ surface. S 2p is a doublet state with spin-orbit splitting of 1.1 eV.[28] For the monolayer spectrum, a good fit is obtained only when a pair of chemically shifted doublets is used. This implies that the S atoms exist in two different chemical environments. For the multilayer spectrum, the low BE peak dominates, so it is assumed that this represents a S atom that is not involved in bonding to the surface. The peak shifted to higher BE by 0.7 eV is therefore attributed to S atoms interacting with the surface. The ratio of these two peaks for the monolayer is 1:1.

Two possible bonding geometries are consistent with the measured data, both involving the interaction of one S atom of a thiocyanate (NCS) ligand with the surface. In the first model, both binding carboxyl groups are on the same bi-isonicotinic acid ligand, while in the second model they are on different bi-isonicotinic acid ligands. The latter is often proposed for the adsorption of N3 on the (101) surface of anatase TiO$_2$,[3] although no real consensus has been reached so far. For the (110) surface of rutile, however, the most plausible bonding geometry is one in which both binding
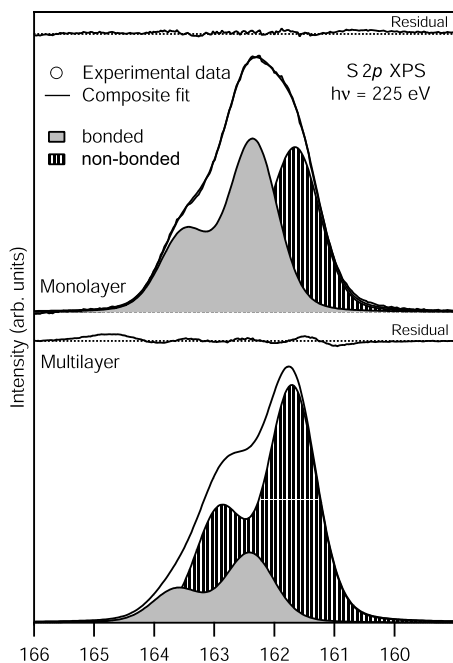
FIG. 4. S 2*p* core-level spectra measured using $h\nu = 225$ eV. Total instrument resolutions were ~50 and 140 meV for the mono- and multilayers, respectively.
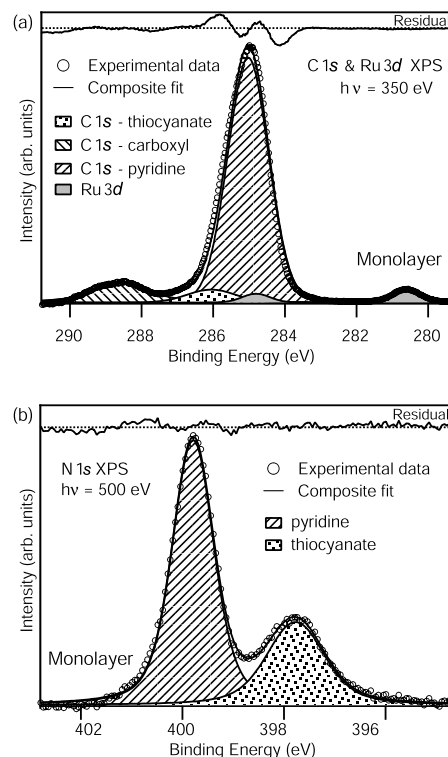

FIG. 5. (a) C 1*s* core-level spectrum measured using $h\nu = 350$ eV, and (b) N 1*s* core-level spectrum measured using $h\nu = 500$ eV. Total instrument resolutions were ~90 and ~140 meV, respectively.

carboxyl groups are located in the same bi-isonicotinic acid ligand, as shown in Fig. 1(a). This has previously been proposed for *ex situ* prepared monolayers of N3 on nanostructured TiO$_2$.[6]

Figure 1(a) represents a geometry optimization of N3 on TiO$_2$(110), calculated using DFT. The structure has one S atom bonded to a surface bridging O atom, and the O atoms of both carboxyl groups from one bi-isonicotinic acid ligand bonded to surface Ti atoms. This represents an overall energy that is 1.1 eV lower than the geometry calculated for the structure in which the two bonding carboxyl groups are on different bi-isonicotinic acid ligands. The additional energy here results from increased strain within the molecule. The proposed model in Fig. 1(a) is also shown in our calculations to be 0.7 eV more stable than a geometry with no S bonded to the surface, consistent with the S 2*p* spectra shown in Fig. 4.

Figure 5(a) shows a photoelectron spectrum of the C 1*s* and Ru 3*d* states for the monolayer, measured using $h\nu = 350$ eV. There are three resolvable chemical environments for C in N3: the pyridine, carboxyl, and thiocyanate groups, in an atomic ratio of 10:2:1, respectively. The ratio found for the monolayer is 10.2:1.2:1, the discrepancy most likely due to half of these groups being bonded to the surface and therefore shadowed by the rest of the molecule. Previous studies of bi-isonicotinic acid—containing the pyridine and carboxyl carbon atoms—were used to identify the peaks.[29,30] As with the O 1*s* data above, all of the features in the spectra can be attributed to N3, which suggests that the surface concentration of any residual methanol from the electrospray beam is very low compared to that of the dye.

Ru 3*d* is a doublet state with spin-orbit splitting of 4.2 eV.[31] The lower BE Ru 3$d_{5/2}$ peak can be seen clearly in the spectrum at 281.4 eV. This is approximately 1.4 eV

higher than metallic ruthenium[31] and is thus consistent with the Ru^{2+} oxidation state of the metal center. This strongly suggests that the molecule has retained its molecular integrity during deposition.

Figure 5(b) shows a N 1*s* photoelectron spectrum of the monolayer measured using $h\nu = 500$ eV. N3 has a ratio of 2(pyridine):1(thiocyanate) N atoms. This is reflected in the 2.3:1 peak intensity ratio found here, providing further evidence that the molecules arrive at the surface in their entirety.

B. Electronic coupling

1. Molecular orbitals

In a DSC, electrons from high-lying occupied molecular orbitals in the dye are photoexcited to previously unoccupied molecular orbitals. For subsequent electron injection into the TiO$_2$ substrate, the unoccupied level of the dye involved in the transfer must overlap with the TiO$_2$ conduction band continuum of states. Spectra representing the occupied and unoccupied states of the N3 monolayer have here been placed on a common BE scale following a procedure outlined elsewhere.[30] This picture is the key in identifying the charge-transfer processes that can occur in the model N3/TiO$_2$ DSC.[32–35]

Figure 6 shows the N 1*s* (Auger yield) NEXAFS and valence PES spectra for a monolayer, along with the clean substrate valence PES (measured at $h\nu = 110$ eV). While the N 1*s* core level (Fig. 5) consists of two peaks, the pyridine N was used to place the NEXAFS on the common BE axis, as it is clear that the N 1*s* NEXAFS is dominated by pyridine-
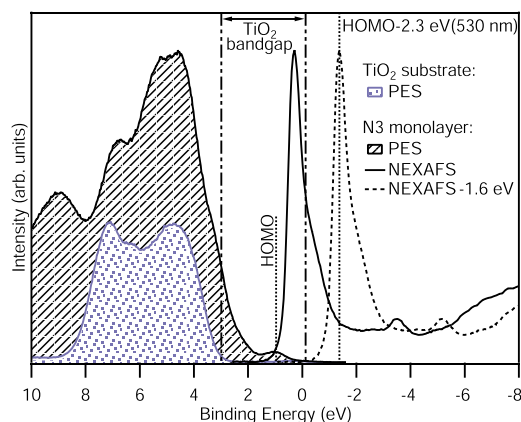
FIG. 6. (Color online) Valence band PES spectra of the clean substrate and of a monolayer of N3, adjacent to a N 1s NEXAFS spectrum of the N3 monolayer. The NEXAFS spectrum is also shown shifted by −1.6 eV to align with the optical HOMO-LUMO gap of 2.3 eV. The optical bandgap of rutile TiO$_2$ (Ref. 16) is also indicated. The PES spectra were measured using $h\nu$=110 eV and had a total instrument resolution of ∼40 meV. The NEXAFS spectrum was taken over the photon energy range $h\nu$ =396.6–425.0 eV and had a photon energy resolution of <170 meV.

like π^* orbitals as seen for the bi-isonicotinic acid ligand on its own.[29,36] Moreover, in our DFT calculations of the N3/TiO$_2$ system, the lowest unoccupied molecular orbital (LUMO) is located on a bi-isonicotinic acid ligand and the central Ru atom, with no intensity on either thiocyanate ligand.

While peaks derived from the bi-isonicotinic acid N atoms are then located energetically in the right place, any peaks deriving from thiocyanate N will appear artificially shifted by approximately 2 eV to higher BE. DFT calculations show several orbitals localized on the thiocyanate ligands which are ∼3 eV lower in BE than the LUMO. The shoulder on the low BE side of the LUMO is attributed to these levels; the peaks would appear 2 eV higher in BE than their calculated energies, placing them ∼1 eV lower in BE than the LUMO, as observed. This shoulder is also the only significant feature in the N 1s NEXAFS spectra that is not present for bi-isonicotinic acid on TiO$_2$. A similar approach has been used elsewhere in interpretation of the C 1s NEXAFS spectra of benzoic acid based on the C 1s BE difference between the phenyl and carboxyl C atoms.[30]

The PES peak at 1.0 eV is the highest occupied molecular orbital (HOMO) and is noteworthy as it narrows the HOMO-LUMO gap, allowing visible light excitations that are fundamental to the DSC mechanism.[3] The HOMO is involved in the initial photoexcitation step within the real DSC.[3] Optical absorption spectra of N3 on TiO$_2$ show maxima, which correspond to photon energies that photoexcite electrons from the HOMO to various unoccupied levels. The lowest in energy of these maxima is centered at a wavelength of 535 nm,[37] which corresponds to a photon energy of 2.3 eV. This is also the absorption maximum with the highest incident-photon-to-current conversion efficiency.[1] The final state of the 535 nm photoexcitation in the real DSC is predicted then to lie 2.3 eV lower in BE than the HOMO. The 535 nm absorption maximum is attributed to the HOMO→LUMO transition, corresponding to a

Ru($4d$)NCS→bpy(π^*)COOH transition. The spatial distributions of the HOMO and LUMO are shown in Fig. 10 and are discussed later in the context of charge transfer dynamics.

In the present case where the unoccupied states are probed using N 1s NEXAFS, a *core* exciton (bound electron-hole pair) is created, whereas in a real DSC a *valence* exciton is created. The presence of a hole in both NEXAFS and optical absorption shifts the unoccupied states to higher BE with respect to the ground state. The BE of the excitons, equivalent to the amount by which the unoccupied levels shift, is attributed to a combination of the Coulomb interaction between the hole and excited electron and the rehybridization of the molecular states upon core- or valence-hole creation.[38] Comparing the HOMO-LUMO gap for optical (2.3 eV) to the HOMO-LUMO gap for the core-excited system (0.7 eV), the difference in energy is 1.6 ± 0.1 eV. This is indicative of the difference between the N 1s core exciton and valence exciton BEs for this molecule. This value is slightly larger than the difference in BE of 1.3 eV found for pyridine,[38] a molecule closely related to the bi-isonicotinic acid ligands of N3. Since the Coulomb attraction of the core hole is responsible for the BE of a core exciton to be larger than that of a valence exciton, this effect is perhaps greater in N3 due to less efficient screening of the N 1s core hole caused by the metal binding to the N atoms.

Shifting the NEXAFS spectrum into alignment with the 2.3 eV optical HOMO-LUMO gap, as shown in Fig. 6, causes the LUMO to lie above the substrate conduction band edge, and thus in a real solar cell would permit electron injection from the LUMO into the substrate. This contrasts with the energy alignment of the core-excited system here, where the LUMO-to-substrate transition is forbidden due to overlap with the substrate bandgap. In the next section, electrons excited to the LUMO are therefore used as a reference, allowing us to probe electron injection from those remaining unoccupied levels that lie above the conduction band edge.[34,39]

2. Electron dynamics

In DSCs, a key step in the photovoltaic process is electron injection from the excited molecule into the substrate conduction band. RPES is used here to investigate molecule-to-substrate charge transfer. This technique enables us to quantify the delocalization of charge from unoccupied molecular orbitals to the conduction band of the substrate on the low femtosecond time scale, as described in the supplementary information,[40] and as previously demonstrated for the bi-isonicotinic acid ligands of N3 on TiO$_2$(110).[34] Essentially, the presence of resonant photoemission and resonant Auger indicates that the electron excited to an unoccupied level in x-ray absorption is still present on the time scale of the core-hole lifetime. This is expected for the multilayer, but for the coupled monolayer (where electrons can delocalize into the substrate conduction band), a reduced intensity of the resonant channels can reveal the extent to which charge injection occurs.
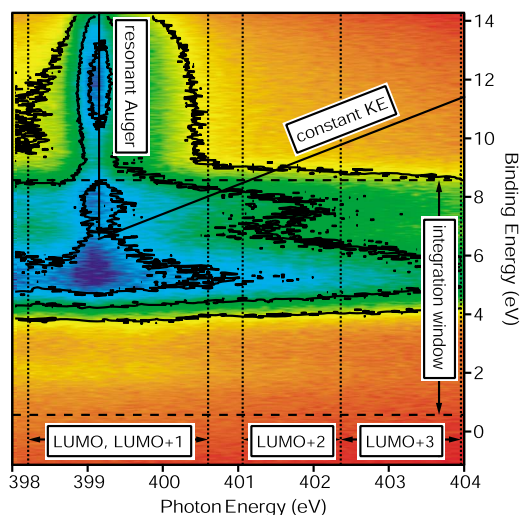
FIG. 7. (Color online) N 1*s* RPES data for the N3/TiO$_2$ monolayer. Valence band spectra with a BE range of 4–20 eV were acquired over the photon energy range $h\nu$=397–405 eV. Photon energy resolution was <170 meV.

Figure 7 shows a two dimensional N 1*s* resonant photo-emission spectrum for the monolayer. The normal and reso-nant Auger peaks (here unseparable—see supplementary information[40]) all occur to higher BE of the "constant KE" line in the figure (linear relationship between $h\nu$ and BE). The line was placed at the low BE limit of the Auger peak at the LUMO, based on a curve fit of the Auger tail minus the pre-edge structure. Any peaks to lower BE of this line then, arise from photoemission and resonant photoemission only.

As discussed in the previous section, the LUMO lies in the substrate bandgap, so electron injection from this level is forbidden. Electron injection is, however, energetically al-lowed from the LUMO+1, LUMO+2, and LUMO+3. As shown in Fig. 7, integrating over a 0.6–8.6 eV BE window includes only photoemission and resonant photoemission over the LUMO+2 and LUMO+3 levels. This integration has been performed for both the multilayer and monolayer, as shown in Fig. 8. Any peaks at the LUMO+2 or LUMO+3 are due solely to resonant photoemission, as normal pho-toemission contributes a sloping background only. The LUMO+1 is not included as it cannot be separated from the LUMO.

In Fig. 8 the RPES spectra are normalized to the LUMO, as are the corresponding NEXAFS spectra which are also shown. In the NEXAFS spectra, the peaks represent the un-occupied levels' full intensities, whereas for RPES, the LUMO has its full intensity but the LUMO+1, LUMO+2, and LUMO+3 may be depleted by charge transfer. For the multilayer it can be seen that the LUMO+2 and LUMO+3 are smaller in the RPES than in the NEXAFS. This ratio is attributed purely to matrix element effects due to the differ-ent techniques used.[33] For the monolayer RPES, however, these peaks have been reduced down to the level of noise, indicating that charge transfer is occurring from these levels.

The core-hole clock implementation of RPES can be used to quantify the electron injection time scales from these levels. The technique uses the fact that if charge transfer is occurring, it must be competing with the de-excitation of the
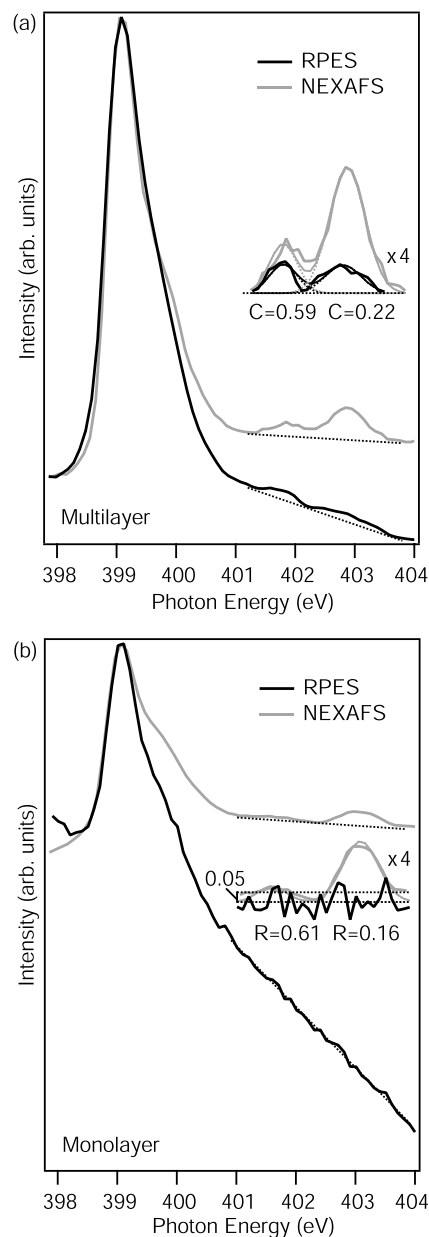

FIG. 8. N 1*s* RPES and N 1*s* NEXAFS spectra of the N3 multilayer and monolayer. The RPES spectra shown here are BE integrations from 0.6 to 8.6 eV over the datasets. Also shown are 4× magnifications of the LUMO+2 and LUMO+3 region. The RPES:NEXAFS intensity ratios for the multilayer are measured to be C_{LUMO+2}=0.59 and C_{LUMO+3}=0.22, and for the monolayer as R_{LUMO+2}=0.61 and R_{LUMO+3}=0.16.

excited state via resonant photoemission or resonant Auger. The time taken for de-excitation here can also be described as the lifetime of the N 1*s* core hole. Here we calculate the electron injection time from the LUMO+3, as this is the most significantly depleted peak. Denoting the intensity of the LUMO+3 as I, the electron injection time τ_{EI} for elec-trons moving from the LUMO+3 to unoccupied substrate states is given by Eq. (1). For a complete discussion of the core-hole clock implementation of RPES, including the deri-vation of this equation, the reader is directed to Brühwiler *et al.*[39] and references therein.

$$\tau_{EI} = \tau_{CH}\frac{I_{RPES}^{mono}/I_{NEXAFS}^{mono}}{I_{RPES}^{multi}/I_{NEXAFS}^{multi} - I_{RPES}^{mono}/I_{NEXAFS}^{mono}}. \quad (1)$$

The variables $I_{\mathrm{RPES}}^{\mathrm{mono}}$ and $I_{\mathrm{RPES}}^{\mathrm{multi}}$ represent the intensities of the LUMO+3 peaks in the RPES monolayer and multilayer, respectively. These values are each normalized by the total cross sections as provided by the NEXAFS intensities $I_{\mathrm{NEXAFS}}^{\mathrm{mono}}$ and $I_{\mathrm{NEXAFS}}^{\mathrm{multi}}$. The variable τ_{CH} is the average N $1s$ core-hole lifetime which has been measured as 6 fs.[41]

It is clear from the monolayer data shown in Fig. 8 that no discernable peak is observed at the position of the LUMO+3. We must therefore take the level of noise as an upper limit for the intensity of any peak that might be present. This will, in turn, give an upper limit for the charge-transfer time according to Eq. (1). Here $I_{\mathrm{RPES}}^{\mathrm{mono}}/I_{\mathrm{NEXAFS}}^{\mathrm{mono}}$ =0.16 and $I_{\mathrm{RPES}}^{\mathrm{multi}}/I_{\mathrm{NEXAFS}}^{\mathrm{multi}}$=0.22, giving an upper time limit of 16 fs as the average electron injection time into the substrate from the LUMO+3. This is in agreement with the electron injection upper time limit for bi-isonicotinic acid on TiO$_2$, which has been found previously to be <3 fs.[34] The electron injection time from N3 to TiO$_2$ has also been measured previously using transient absorption spectroscopy, giving instrument-limited upper time limits ranging from 50 to 150 fs.[42–44] While such techniques operating in the time domain are limited by the time scale of pulsed laser sources ($\sim$50 fs in the cited works), the core-hole clock method operates in the energy domain and is limited by the core-hole lifetime (typically a few femtoseconds).

That $I_{\mathrm{RPES}}^{\mathrm{multi}}/I_{\mathrm{NEXAFS}}^{\mathrm{multi}}$ is 0.22 and not 0.3 as found for bi-isonicotinic acid[34] can perhaps be attributed to ultrafast delocalization of excited electrons *within* the molecule. Such intrinsic delocalization would lead to reduced resonant photoemission even in the absence of charge-transfer to the substrate. Evidence of ultrafast intramolecular delocalization has previously been found in the RPES of a related ruthenium complex comprising three bipyridine ligands, for which little or no resonant photoemission was measured for resonances lying higher than the LUMO in the multilayer.[45] The $I_{\mathrm{RPES}}^{\mathrm{multi}}/I_{\mathrm{NEXAFS}}^{\mathrm{multi}}$ ratio of 0.22 for the multilayer can therefore be interpreted as a combination of the aforementioned matrix element effect and intramolecular delocalization. In the case of the monolayer, a fraction of the electrons that are localized in the multilayer are able to charge transfer into the substrate, bringing the RPES/NEXAFS ratio from 0.22 down to 0.16, and it is these injected electrons that are investigated in the RPES analysis. In other words, intramolecular delocalization is accounted for in Eq. (1) through the experimentally measured value of $I_{\mathrm{RPES}}^{\mathrm{multi}}/I_{\mathrm{NEXAFS}}^{\mathrm{multi}}$.

In the previous section, it was concluded that the LUMO is actively involved in the DSC photovoltaic process. Since in the RPES technique the unoccupied levels are excitonically pulled down into the TiO$_2$ bandgap, we are unable to probe the LUMO or LUMO+1 electron injection times directly. However, as also discussed in the previous section and supported by preliminary DFT calculations, the LUMO and LUMO+3 are both thought to be located on the bi-isonicotinic acid ligands. It is therefore reasonable to assume that the coupling of these orbitals to the substrate and, therefore, the corresponding charge-transfer dynamics, will be similar. This gives some insight into why the N3 DSC is so efficient.
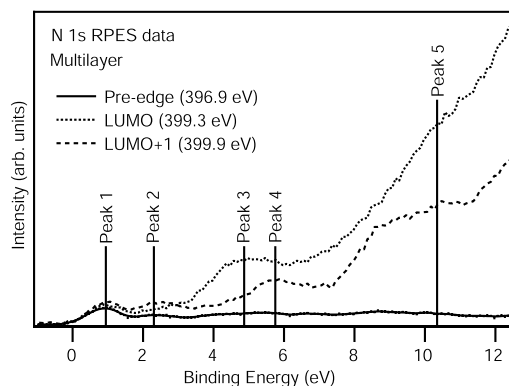

FIG. 9. Photon energy slices of the multilayer RPES data taken at pre-edge, LUMO, and LUMO+1 photon energies to give a clearer view of the misaligned peaks.

An interesting characteristics of the RPES data is that the photoemission enhancements observed at the LUMO resonance occur at different BEs to those observed at the LUMO+1 resonance. This is demonstrated by comparing the resonant photoemission measured at the LUMO and LUMO+1 absorption energies, as shown in Fig. 9. Here the enhancement of peak 1—the HOMO—can be seen primarily at the LUMO+1 position rather than the LUMO. Similarly, peak 3 is enhanced only at the LUMO resonance, while peaks 2, 4, and 5 occur only for the LUMO+1.

For resonant photoemission to occur following core excitation, the occupied (BE scale) and unoccupied ($h\nu$ scale) orbitals involved must have some interactions. Moreover, the largest probability for resonant photoemission will be when both electrons involved (i.e., the one that fills the core hole, and the emitted Auger-type electron) are located on the same atom, specifically the site of the core hole. Resonant photoemission is in essence a special type of Auger decay, and while interatomic Auger transitions can occur,[46] the rates of these events are negligible in all but the lowest energy Auger processes. The origin of the state-dependent resonant enhancements observed for the occupied molecular orbitals observed in Fig. 9 is therefore likely to be due to the spatial distribution of both the occupied and unoccupied orbitals involved in the core-hole decay process. More specifically, the results suggest that the LUMO and LUMO+1 are located on different parts of the molecule, in agreement with the previous section, where the LUMO was attributed to the bi-isonicotinic acid ligands and the LUMO+1 to the thiocyanate ligands. This is also supported by the DFT calculations (as described in Sec. II) shown in Fig. 10 which illustrate the spatial distribution of some of the occupied and unoccupied orbitals of a free N3 molecule. The orbitals are labeled with their calculated energies in inverted commas to remind the reader that these are theoretically calculated values and are not experimentally measured quantities. Shown in Fig. 10 are the HOMO ("0.0 eV"), LUMO ("1.2 eV"), and the unoccupied level at "3.3 eV." The latter is attributed to the LUMO+1 resonance observed at 399.9 eV in the N $1s$ NEXAFS for reasons outlined in the previous section.

The state-dependent enhancements of the HOMO, in Fig. 9 can be understood in terms of their spatial distribution
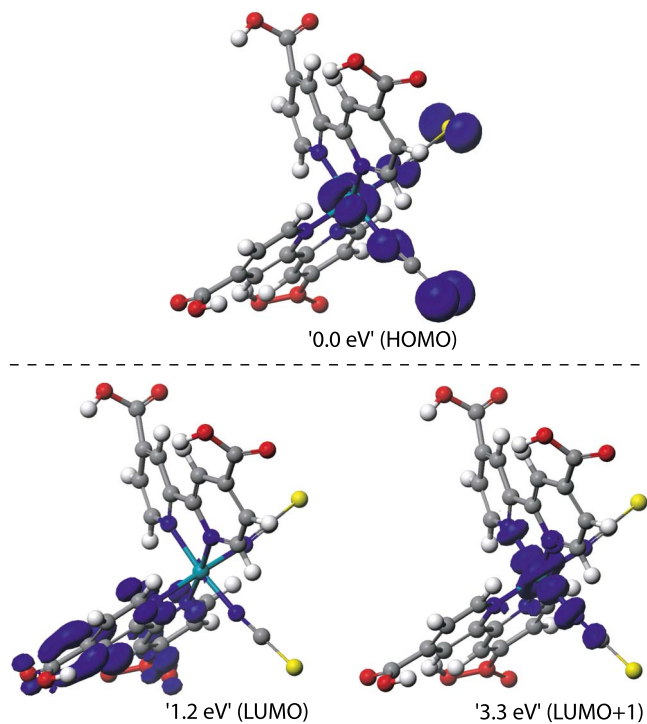
FIG. 10. (Color online) DFT calculations showing electron orbitals of a geometry-optimized free N3 molecule.

within the molecule and the location of the core-hole site in each of the LUMO and LUMO+1 excitations. Since the HOMO has no intensity on the N atoms of the bi-isonicotinic acid ligand, there is a negligible probability of an electron from this orbital playing any role in the participator decay (resonant photoemission) of the core-hole created on excitation to the LUMO (localized as shown in Fig. 10 on the bi-isonicotinic ligand). Indeed, there is little or no enhancement of the HOMO at the LUMO energy (399.3 eV) in Fig. 9 above the pre-edge direct photoemission spectrum. Conversely, an electron from the HOMO can participate in the decay of the N 1s core-hole created on excitation to the LUMO+1 located on the thiocyanate ligand. A small resonant enhancement of the HOMO is therefore observed in Fig. 9 at the LUMO+1 photon energy (399.9 eV). An analogous mechanism is proposed for the state-dependent enhancements of the other valence states observed in Fig. 9. Those occupied states located primarily on the thiocyanate ligands are able to play a role in the participator decay of the N 1s-LUMO+1 core-excited state, while those local to the bi-isonicotinic acid ligands contribute to the decay of the N 1s-LUMO state.

It is worth noting that while both the HOMO and LUMO would need some degree of overlap with the core-excited atom in order to give rise to resonant photoemission, only an overlap with one another is required for the HOMO-LUMO photoexcitation in a real solar cell. Close inspection of the calculated LUMO in Fig. 10 reveals a small contribution to the central Ru atom of the molecule. The photoexcitation channel between the two orbitals is therefore facilitated by their overlap at the center of the molecule.

IV. CONCLUSIONS

UHV electrospray deposition has been used to deposit monolayers and multilayers of N3 on the rutile TiO$_2$(110) surface *in situ*. PES has been used to characterize core and valence levels of the system, which were then used to deduce the bonding geometry of a monolayer of N3 chemisorbed to TiO$_2$(110). We find that the carboxyl groups of one bi-isonicotinic acid ligand deprotonate so that its O atoms bond to Ti atoms of the substrate, and one of the thiocyanate groups bonds via a S atom to an O atom of the substrate. DFT calculations indicate that this geometry is energetically more favorable than the bonding of one carboxyl group from each bi-isonicotinic acid ligand.

The energetic alignment of the system was determined by placing the valence PES and N 1s NEXAFS of an N3 monolayer onto a common BE scale. The bandgap of TiO$_2$(110) was aligned using the valence PES of the clean substrate. The 535 nm optical absorption maximum of N3 on TiO$_2$ was attributed to the HOMO→LUMO transition in a working solar cell. This was used to compare the energetics as they would appear for photoexcitation from the valence band (as occurs in the working N3 DSC) with those found for photoexcitation from the N 1s core level, for which the unoccupied levels appear at a higher BE. This comparison allowed quantification of the difference in BE of a core and valence excitation for this system, found to be 1.6 ± 0.1 eV.

The core-hole clock implementation of RPES was used to find that electron injection from the LUMO+3 to the substrate occurs in <16 fs, in agreement with the previous studies of bi-isonicotinic acid and related molecules on TiO$_2$ which found charge transfer to occur in <3 fs. The LUMO and LUMO+3 are both thought to be located on the bi-isonicotinic acid ligands, so electron injection in the real DSC is expected to be in a similar time scale.

In the RPES data, resonant photoemission peaks are seen only for certain occupied-unoccupied level combinations due to the spatial distribution of the molecular orbitals and their overlap with each other and the core-hole site. Combined with DFT calculations we can understand this process for the state-dependent enhancement of the HOMO at the excitation energies of the LUMO and LUMO+1 resonances. The HOMO and LUMO+1 are localized at the central Ru atom and thiocyanate ligands, while the LUMO is localized largely at the bipyridine (π^*) and carboxyl groups.

[1] M. Grätzel, Nature (London) **414**, 338 (2001).

[2] M. Grätzel, Philos. Trans. R. Soc. London **365**, 993 (2007).

[3] M. Grätzel and A. Hagfeldt, Acc. Chem. Res. **33**, 269 (2000).

[4] M. Grätzel, J. Photochem. Photobiol., A **164**, 3 (2004).

[5] H. Rensmo, S. Södergren, L. Patthey, K. Westermark, L. Vayssieres, O. Kohle, P. Brühwiler, A. Hagfeldt, and H. Siegbahn, Chem. Phys. Lett. **274**, 51 (1997).

[6] E. M. J. Johansson, M. Hedlund, H. Siegbahn, and H. Rensmo, J. Phys. Chem. B **109**, 22256 (2005).

[7] S. Wendt, R. Schaub, J. Matthiesen *et al.*, Surf. Sci. **598**, 226 (2005).

[8] J. E. Lyon, A. J. Cascio, M. M. Beerbom, R. Schlaf, Y. Zhu, and S. A. Jenekhe, Appl. Phys. Lett. **88**, 22 (2006).

[9] J. C. Swarbrick, J. B. Taylor, and J. N. O'Shea, Appl. Surf. Sci. **252**, 5622 (2007).

[10] S. Rauschenbach, F. Stadler, E. Lunedei, N. Malinowski, S. Koltsov, G. Costantini, and K. Kern, Small **2**, 540 (2006).

[11] J. N. O'Shea, J. B. Taylor, J. C. Swarbrick, G. Magnano, L. C. Mayor, and K. Schulte, Nanotechnology **18**, 035707 (2007).

[12] C. J. Satterley, L. M. A. Perdigão, A. Saywell, G. Magnano, A. Rienzo, L. C. Mayor, V. R. Dhanak, P. H. Beton, and J. N. O'Shea, Nanotechnology **18**, 455304 (2007).

[13] A. Saywell, G. Magnano, C. J. Satterley, L. M. A. Perdigão, N. R. Champness, P. H. Beton, and J. N. O'Shea, J. Phys. Chem. C **112**, 7706 (2008).

[14] L. Patthey, H. Rensmo, P. Persson *et al.*, J. Chem. Phys. **110**, 5913 (1999).

[15] A. Thomas, W. Flavell, C. Chatwin, S. Rayner, D. Tsoutsou, A. Kumarasinghe, D. Brete, T. Johal, S. Patel, and J. Purton, Surf. Sci. **592**, 159 (2005).

[16] D. C. Cronemeyer, Phys. Rev. **87**, 876 (1952).

[17] B. O'Regan and M. Grätzel, Nature (London) **353**, 737 (1991).

[18] R. Denecke, P. Vaterlein, M. Bassler, N. Wassdahl, S. Butorin, A. Nilsson, J. E. Rubensson, J. Nordgren, N. Mårtensson, and R. Nyholm, J. Electron Spectrosc. Relat. Phenom. **101–103**, 971 (1999).

[19] U. Diebold, Surf. Sci. Rep. **48**, 53 (2003).

[20] A. M. G. nàn Calvo, Phys. Rev. Lett. **79**, 217 (1997).

[21] S. J. Gaskell, J. Mass Spectrom. **32**, 677 (1997).

[22] J. Schnadt, J. N. O'Shea, L. Patthey, J. Schiessling, J. Krempaský, M. Shi, N. Mårtensson, and P. A. Brühwiler, Surf. Sci. **544**, 74 (2003).

[23] M. D. Segall, P. J. D. Lindan, M. J. Probert, C. J. Pickard, P. J. Hasnip, S. J. Clark, and M. C. Payne, J. Phys.: Condens. Matter **14**, 2717 (2002).

[24] J. Schnadt, J. Schiessling, J. N. OShea *et al.*, Surf. Sci. **540**, 39 (2003).

[25] J. N. O'Shea, Y. Luo, J. Schnadt, L. Patthey, H. Hillesheimer, J. Krempaský, D. Nordlund, M. Nagasono, and N. Mårtensson, Surf. Sci. **486**, 157 (2001).

[26] J. N. O'Shea, J. Schnadt, P. A. Brühwiler, H. H. N. Mårtensson, L. Patthey, J. Krempaský, C. Wang, Y. Luo, and H. Ågren, J. Phys. Chem. B **105**, 1917 (2001).

[27] J. N. O'Shea, J. C. Swarbrick, K. Nilson, C. Puglia, B. Brena, Y. Luo, and V. R. Dhanak, J. Chem. Phys. **121**, 10203 (2004).

[28] A. C. Thompson, D. T. Attwood, E. M. Gullikson *et al.*, *Centre for X-ray Optics Advanced Light Source-X-ray Data Booklet* (Lawrence Berkeley National Laboratory, California, 2001).

[29] J. N. O'Shea, J. B. Taylor, L. C. Mayor, J. C. Swarbrick, and J. Schnadt, Surf. Sci. **602**, 1693 (2008).

[30] J. Schnadt, J. N. O'Shea, L. Patthey, J. Krempaský, N. Mårtensson, and P. A. Brühwiler, Phys. Rev. B **67**, 235420 (2003).

[31] J. C. Fuggle and N. Mårtensson, J. Electron Spectrosc. Relat. Phenom. **21**, 275 (1980).

[32] J. B. Taylor, L. C. Mayor, J. C. Swarbrick, J. N. O'Shea, C. Isvoranu, and J. Schnadt, J. Chem. Phys. **127**, 134707 (2007).

[33] J. B. Taylor, L. C. Mayor, J. C. Swarbrick, J. N. O'Shea, and J. Schnadt, J. Phys. Chem. C **111**, 16646 (2007).

[34] J. Schnadt, P. A. Brühwiler, L. Patthey *et al.*, Nature (London) **418**, 620 (2002).

[35] J. Schnadt, J. N. O'Shea, L. Patthey *et al.*, J. Chem. Phys. **119**, 12462 (2003).

[36] P. Persson, S. Lunell, P. A. Brühwiler, *et al.*, J. Chem. Phys. **112**, 3945 (2000).

[37] P. Myllyperkiö, G. Benkö, J. E. I. Korppi-Tommola, A. P. Yartsev, and V. Sundström, Phys. Chem. Chem. Phys. **10**, 996 (2007).

[38] J. Schnadt, J. Schiessling, and P. Brühwiler, Chem. Phys. **312**, 39 (2005).

[39] P. A. Brühwiler, O. Karis, and N. Mårtensson, Rev. Mod. Phys. **74**, 703 (2002).

[40] See EPAPS Document No. E-JCPSA6-129-606835 for more detailed information about the core-hole clock implementation of resonant photoemission. For more information on EPAPS, see http://www.aip.org/pubservs/epaps.html.

[41] B. Kempgens, A. Kivimäki, M. Neeb, H. M. Köppe, A. M. Bradshaw, and J. Feldhaus, J. Phys. B **29**, 5389 (1996).

[42] S. Deb, R. Ellingson, S. Ferrere, A. Frank, B. Gregg, A. Nozik, N. Park, and G. Schlichthörl, NREL Report No. CP-590-25056 (1998).

[43] A. Furube, M. Murai, S. Watanabe, K. Hara, R. Katoh, and M. Tachiya, J. Photochem. Photobiol., A **182**, 273 (2006).

[44] Y. Tachibana, J. E. Moser, M. Grätzel, D. R. Klug, and J. R. Durrant, J. Phys. Chem. **100**, 20056 (1996).

[45] K. Westermark, H. Rensmo, J. Schnadt, P. Persson, S. Södergren, P. Brühwiler, S. Lunell, and H. Siegbahn, Chem. Phys. **285**, 167 (2002).

[46] J. A. D. Matthew and Y. Komninos, Surf. Sci. **53**, 716 (1975).